



The influence of residual thermal stresses on the mechanical properties of multilayer α -Al₂O₃/TiC_xN_{1-x} coatings on WC/Co cutting tools

Harry Chien^a, Carlos Diaz-Jimenez^a, Gregory S. Rohrer^{a,*}, Zhigang Ban^b, Paul Prichard^b, Yixiong Liu^b

^a Department of Materials Science and Engineering, Carnegie Mellon University, Pittsburgh, PA 15213, United States

^b Kennametal Incorporated, 1600 Technology Way, P.O. Box 231, Latrobe, PA 15650, United States

ARTICLE INFO

Available online 6 November 2012

Keywords:

Thermal stresses

Al₂O₃

TiC_xN_{1-x}

Hardness

Microstructure

Channel cracks

ABSTRACT

Orientation maps of the microstructures of four α -Al₂O₃ and TiC_xN_{1-x} multilayer coatings on WC–Co cemented carbide tool bit inserts were used to create realistic models for finite element calculations of residual thermal stresses. The calculations show that channel cracks in the coatings relieve thermal stresses and that the amount of stress relieved increases with film thickness. The hardness and fracture toughness of the coatings, measured by nano-indentation, are inversely correlated to the calculated mean thermal stress, where the hardest sample has the smallest calculated mean thermal stress. The calculations also indicate that cracks spaced more closely than about 50 μ m are not effective in further reducing residual stresses.

© 2012 Elsevier B.V. All rights reserved.

1. Introduction

Multilayer coatings are often used to improve the lifetime, performance, and wear resistance of composite cutting tools. In this paper, residual thermal stresses in α -Al₂O₃/TiC_xN_{1-x} coatings deposited by chemical vapor deposition on WC–Co cemented carbides are calculated and compared to measured hardnesses. In these multilayer systems, the α -Al₂O₃ and TiC_xN_{1-x} coating layers are less than 30 μ m thick. The coatings are usually capped by a much thinner TiN layer (<1 μ m thick) that will not be considered further in this paper. These coatings are representative of the most commonly used coatings in cutting tool applications [1].

CVD coatings are typically deposited at a temperature greater than 800 °C. Residual thermal stresses occur in these coatings after cooling for two reasons. One is the anisotropic thermal expansion coefficients in the alumina layer; misoriented crystals contract by different amounts upon cooling and create a range of tensile and compressive stresses [2]. The second source of residual stress is the mismatch in the thermal expansion coefficients of the substrate and coating materials [3]. Because the thermal expansion coefficients of the coating materials are larger than the thermal expansion coefficient of the substrate, they shrink more than the substrate during cooling in the unconstrained state. However, because the coatings must conform to the substrate shape in the real material, they are loaded in tension after cooling. Under typical conditions, these thermal stresses exceed the coatings' strength and vertical channel cracks are formed that partially relax the stress. In analogy to bulk polycrystalline alumina, the mean value and distribution of the stored elastic energy in the

coatings is expected to be influenced by the texture in the α -Al₂O₃ layer [2]. Previous calculations of thermal stresses have shown that coatings with [0001] textured α -Al₂O₃ along the film growth direction have less stored elastic energy and coatings with weaker texture have a broader distribution of thermal stresses [3].

Previous models for the thermal stresses in these multilayer coatings have not included the effect of the vertical channel cracks that form on cooling [3]. While it is known that the cracks relieve stress, the distribution of stress and the effect on each coating layer has not been studied. Residual stress measurements by X-ray diffraction are able to provide an average value, but the cracks are expected to relieve stresses in an inhomogeneous way. Because both the cracks and the residual stresses impact the mechanical properties of the coating, it is important to have a model that includes the heterogeneous characteristics of the material.

It should be noted that the above description of residual stresses ignores the intrinsic stresses (sometimes referred to as quenching stresses) that develop during film growth [4]. Intrinsic stresses can be related to defects such as grain boundaries [5] and can occur in physical or chemical vapor deposition processes [6]. Intrinsic stresses can be either tensile or compressive and can even reverse sign during growth [4]. The measurement of intrinsic stresses in thermal barrier coatings indicates that they are smaller than the thermal stresses [7]. The models in this paper simulate only the thermal stresses but the stresses in real coatings are also likely influenced by smaller intrinsic stresses.

Residual thermal stresses in coatings are most commonly determined by measuring the curvature of the substrate film combination [7,8], X-ray diffraction [9], Raman spectroscopy [10,11], or piezospectroscopic methods [12]. In general, these methods yield a single mean stress rather than distributions of stresses. Under the assumption that the films are

* Corresponding author.

E-mail address: rohrer@cmu.edu (G.S. Rohrer).

Table 1
Summary of microstructural characteristics of the coatings.

Layer	Sample	Grains	Grain area, μm^2	Major axis, μm	Minor axis, μm	Thickness, μm
$\text{TiC}_{1-x}\text{N}_x$	1	5538	2.1	4.85	0.67	18.2
	2	1112	1.6	3.46	0.69	6.8
	3	1996	1.93	4.83	0.54	15.0
	4	2050	3.34	5.03	0.79	5.82
Al_2O_3	1	950	2.05	3.08	0.84	11.8
	2	2567	3.9	3.36	1.36	9.2
	3	1151	3.95	4.79	0.99	9.9
	4	568	3.89	4.34	1.07	1.3

homogeneous, elastic stresses can be calculated using analytic methods [13,14]. More recently, image based finite element methods have been applied and those that include the microstructure have the advantage of being able to predict local stresses and the distributions of stresses [3,15].

The goal of this paper is to test the hypothesis that the mechanical properties of the coating can be quantitatively correlated with the residual thermal stresses. One can imagine that if a tensile stress is applied to a coating, it will become less resistant to penetration and have a reduced hardness. Conversely, in compression it should better resist penetration and have an increased hardness. In fact, this has been experimentally observed for some metals [9,16]. In the present case, microstructure might also influence hardness, but an earlier study noted no systematic influence [17]. Therefore, it is reasonable to expect that thermal stress might have a dominant influence. Four typical coatings were selected as examples and the hardnesses and the fracture toughnesses were determined by nano-indentation. Detailed microstructural observations of the same samples were used to develop models of the coatings and the residual thermal stresses were then calculated using the finite element method. By comparing the calculated thermal stresses in each multilayer coating with the measured hardness and fracture toughness, it is possible to show that the quantities are correlated.

2. Experimental methods

The microstructures and hardnesses of the four coated tool bit inserts considered here were described in two earlier publications [3,17]. In the present paper, we consider the same specimens, referred to as samples 1 through 4. All of the specimens are commercially available tool bit inserts and consisted of a WC–Co cemented carbide substrate covered by a $\text{TiC}_x\text{N}_{1-x}$ layer (6.8 μm to 18.2 μm thick) with x approximately equal to 0.5, which was in turn covered by an $\alpha\text{-Al}_2\text{O}_3$ layer (1.3 μm to 11.8 μm thick). Finally, all of the

samples were capped by an approximately 1 μm thick TiN layer (this layer was not characterized). The layers were highly crystalline, yielding electron backscatter diffraction patterns. The layer thicknesses and the mean size and shapes of the grains (the lengths of the major and minor axes of ellipses fit the grains) are listed in Table 1. The grain size and shape parameters were derived from electron backscatter diffraction maps, as described in detail in reference [17]. The specimens were selected because they are typical of coatings in use today. Furthermore, they span the range of total thickness from 7 (sample 4) to 30 (sample 1) μm . The microstructural data reported in the previous papers will be used as input to thermal stress calculations by the finite element method. Furthermore, we report additional measurements of the spacing of thermal stress induced channel cracks and the fracture toughness of the coating.

Typical images of the channel cracks are shown in Fig. 1. To characterize the average spacing of the channel cracks, the number of cracks along the length of a cross-section of each tool bit insert were counted using high magnification imaging in the scanning electron microscope (SEM). Only those cracks that penetrated the thickness of the coating were included (see Fig. 1b).

Hardness measurements were carried out by nano-indentation. To prepare the sample, the tool bit inserts were ground and polished at an approximate angle of 2° with respect to the surface of the coating so that when viewed from the top, extended regions, approximately 200 μm wide and the length of the sample, of each coating layer are visible. This makes it possible to make indents (nearly) normal to the plane of each coating. The grinding was carried out with abrasives from 200 to 1600 grit size and polishing was carried out with 3 μm and 0.5 μm alumina slurries. Hardness measurements were made using a nano-indenter XP (MTS systems corporation) equipped with a Berkovich diamond tip. The diamond tip was calibrated using measurements on fused silica. The hardness and modulus were determined using the standard practice for instrumented indentation testing. For all measurements, the indenter approach rate was 25 nm/s. Once the indenter contacted the surface, the load on the sample increased to a maximum of 10 mN within the time span of 25 s. The maximum load was then held constant for 10 s. Finally, the indenter was withdrawn at twice the loading rate. The maximum depth of indentation was 2 μm . Approximately 30 indents were made in the exposed alumina and $\text{TiC}_x\text{N}_{1-x}$ layer of each sample and the results of these measurements were used to determine mean and standard deviation for the hardness.

An atomic force microscope (Thermomicroscopes M5, Sunnyvale, CA), working in contact mode, was used to image the indents, and it was found that cracks frequently extended from the corners of the triangular indents in the alumina layer. The lengths of the cracks

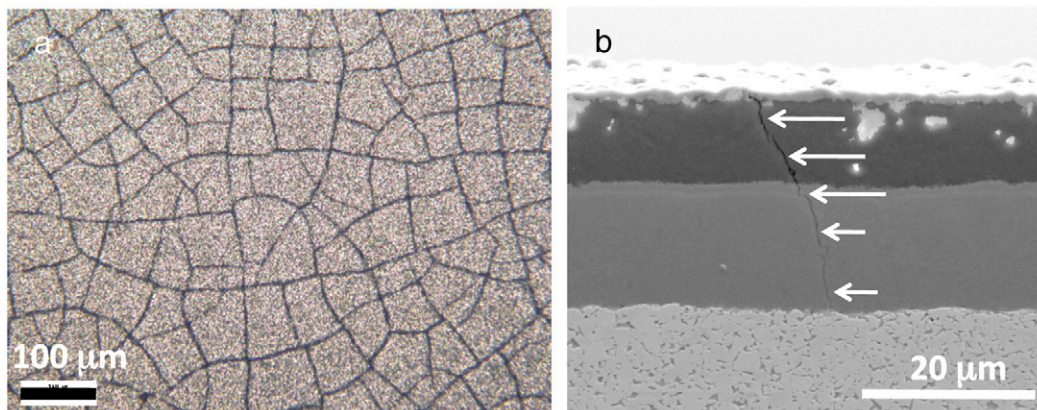


Fig. 1. Images of the channel cracks in CVD deposited coatings. (a) Plan view optical image of the pattern of cracks. (b) SEM image of a cross-section of a coating showing, from top to bottom, the $\alpha\text{-Al}_2\text{O}_3$, $\text{TiC}_x\text{N}_{1-x}$, and WC/Co substrate. The position of the crack is highlighted by the arrows.

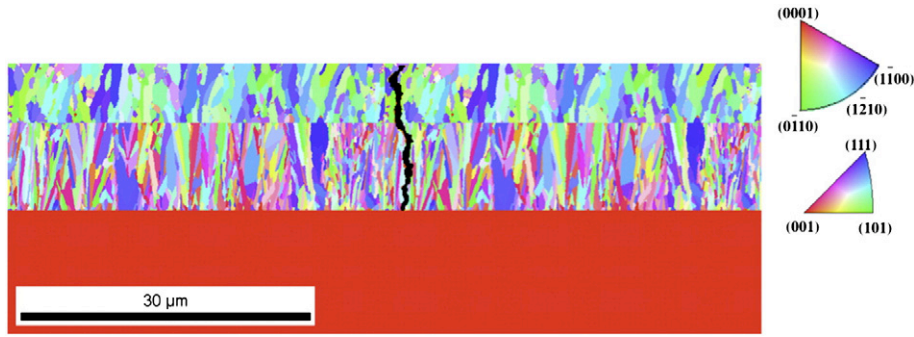


Fig. 2. An example of a microstructure model constructed from observed orientation maps that have been merged so that the length is equal to the average crack spacing. A simulated crack (black) has been added. From top to bottom, the maps of the alumina, $\text{TiC}_x\text{N}_{1-x}$, and substrate, respectively, are assigned the properties associated with those phases. The legends on the right define the orientation–color relationship for the two coating phases.

were measured from the images. The corner cracks that obviously interacted with pre-existing channel cracks were excluded from the analysis. For the four different coatings, at least 10 cracks from 15 images of each sample contributed to the average. Following previously established methods [18,19], the average crack length was used to calculate the fracture toughness using the following relationship:

$$K_c = 1.076X_v \left(\frac{a}{l}\right)^{1/2} \left(\frac{E}{H}\right)^{2/3} \left(\frac{P}{c^{3/2}}\right) \quad (1)$$

where K_c is the fracture toughness, X_v is the empirical constant 0.015 [20], a is the distance between the center of the indent to any of the tip corners, c is the crack length that extends from the corner of the indent, l is the overall crack length ($c + a$), E is the elastic modulus, H is the hardness, and P is the maximum load. In this case, $P = 766$ mN and $a = 7.5$ μm and measured values of the modulus, hardness, and crack length are used for the other parameters. This analysis was carried out only for the indents in the alumina layer. It should be noted that the use of indentation to determine toughness is controversial; it has been shown that toughnesses determined by indentation are not comparable to those determined by standard tests [21]. However, given the physical form of the coatings, this is the only current option for producing quantitative data.

The thermal stresses were calculated using the OOF2 software package (OOF2, version 2.0.5a11, National Institute of Standards and

Technology, Gaithersburg, MD) [22–24]. This software accepts image data as input and here we use the orientation maps reported previously [17]. The code produces meshes from the images and uses the finite element method to compute stresses and strains [24]. This software has been used to simulate a wide range of phenomena in ceramics [25–30] and in this case was validated by comparing the results from simple homogeneous models to independent calculations of the residual thermal stress. The models were constructed by joining orientation maps of the $\alpha\text{-Al}_2\text{O}_3$ and $\text{TiC}_x\text{N}_{1-x}$ layers and placing them on a microstructurally homogeneous substrate. The orientation maps were duplicated as necessary to build structures whose lengths were equal to the average spacing between the channel cracks while maintaining film thicknesses that were measured in the cross-sectional SEM images. A vertical channel crack was simulated in the center of each model by assigning a continuous path of pixels to have crack-like properties (near zero modulus and zero thermal expansion). The creation of the simulated crack begins by converting 2 pixels in the center of the image and at the top of the coating to be part of the crack. To advance the crack toward the substrate, a random number between 0 and 1 is selected. If the number is less than 1/3, the crack advances 1 pixel downward and 1 pixel to the left. If the number is greater than 2/3, the crack

Table 2
Physical properties of the materials used for the simulations.

Material	Young's modulus (GPa)	Poisson's ratio	Coefficient of thermal expansion ($\times 10^{-6}$, K^{-1})	Elastic constants (GPa)
TiN	–	–	9.35 ^a	$C_{11} = 625$, $C_{12} = 165$, $C_{44} = 163$, $A = 0.709$ ^b
TiC	–	–	7.4 ^c	$C_{11} = 513$, $C_{12} = 106$, $C_{44} = 178$, $A = 0.875$ ^d
Al_2O_3	–	–	$a_{11} = 7.67$, $a_{33} = 8.52$ ^e	$C_{11} = 497$, $C_{12} = 163$, $C_{13} = 116$, $C_{14} = 22$, $C_{33} = 501$, $C_{44} = 147$ ^f
WC	619.5	0.24	$a_{11} = 5.2$, $a_{33} = 7.3$ ^g	$C_{11} = 720$, $C_{12} = 254$, $C_{13} = 267$, $C_{33} = 972$, $C_{44} = 328$ ^g
Co	211 ^g	0.31 ^g	14.0 ^g	–
Crack	0.01	0.01	0	–

^a Ref. [31].

^b Ref. [32].

^c Ref. [33].

^d Ref. [34].

^e Ref. [35] at 1100 K.

^f Refs. [36,37].

^g Refs. [16,38,39].

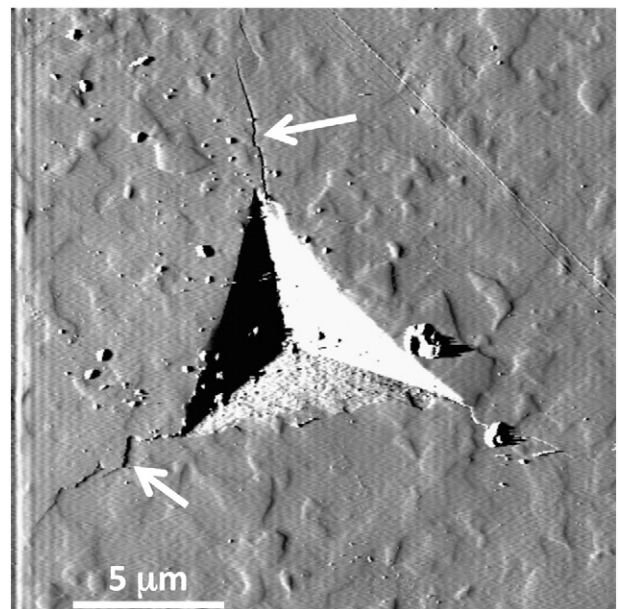


Fig. 3. AFM deflection image of an indent in the alumina layer with cracks protruding from the corners. The cracks are indicated by white arrows.

Table 3

Summary of measured properties of the coatings. Values in parentheses are standard deviations of measured quantities.

		Sample 1	Sample 2	Sample 3	Sample 4
Coating	Average channel crack spacing, μm	129	81	131	96
$\text{TiC}_x\text{N}_{1-x}$	Thickness, μm	18.2	6.8	15.0	5.82
	Modulus, GPa	497 (33)	467 (18)	486 (24)	463 (27)
	Hardness, GPa	21.8 (0.8)	20.8 (1.0)	21.7 (0.7)	20.3 (0.7)
$\alpha\text{-Al}_2\text{O}_3$	Thickness, μm	11.8	9.2	9.9	1.3
	Modulus, GPa	521 (39)	486 (25)	428 (20)	412 (20)
	Hardness, GPa	24.6 (2.2)	24.2 (1.3)	22.3 (1.2)	21.1 (1.4)
	Indenter crack length, μm	4.3 (1.5)	4.7 (1.6)	5.4 (2.3)	7.3 (2.4)
	Fracture toughness, $\text{GPa}\cdot\text{m}^{1/2}$	7.5 (1.6)	6.2 (0.9)	4.6 (0.3)	2.8 (0.5)

advances 1 pixel downward and one step to the right. For all other values, the crack moves downward in a straight line. This procedure causes the crack to meander in a way that is similar to the observed cracks. As an example, one such model is shown in Fig. 2. Cracks generated in this way are qualitatively similar to observed channel cracks.

Microstructure models created as described above were meshed using OOF2 [23]. Each discrete element was assigned a phase and orientation based on the orientation map. The thermal and elastic properties of each phase were assigned according to the data in Table 2. The properties of the $\text{TiC}_x\text{N}_{1-x}$ were estimated based on the properties of the pure binary phases. Because x is approximately 0.5 in these coatings, the coefficient of thermal expansion (CTE) for $\text{TiC}_x\text{N}_{1-x}$ is assumed to be the average of TiN and TiC, which is $8.375 \times 10^{-6} \text{ K}^{-1}$. Each of the elastic constants was also averaged (by averaging the individual components of the stiffness matrix that are listed in Table 2). The elastic properties of the substrate were estimated by averaging the properties of WC and Co according to the volume fractions in the composite.

The boundary conditions of the simulation were set based on the assumption that the coating must conform to the substrate. Therefore, the CTE of the substrate was taken to be zero and the CTEs for the $\alpha\text{-Al}_2\text{O}_3$ and $\text{TiC}_x\text{N}_{1-x}$ were reduced by the CTE of the substrate. The left, right, and bottom of the model were assigned zero

displacement and zero force boundary conditions. The system was then cooled by 800°C (simulating the cooling that occurs from the process temperature to ambient temperature) and the resulting stress and strain were calculated in each element. Using these data, it was also possible to determine the elastic energy distribution by computing the product of the stress and strain in each element. The domain of the computation ranges from 13,000 to 25,000 elements depending on the size of the image. Calculations based on the same models with 50% more or 50% fewer elements yielded the same results.

3. Results

An AFM deflection image of an indent in an alumina layer is shown in Fig. 3. This is an example of one of the indents used for the hardness measurement, obtained from a tool bit insert polished at a 2° angle from the plane of the coating, as described in Section 2. The image reflects the difference between the true deflection and the set point deflection of the cantilever during contact imaging. Black contrast corresponds to deflection below the set point (a negative slope on the surface), white contrast corresponds to deflection greater than the set point (a positive slope on the surface), and gray contrast corresponds to the set point deflection (a flat surface). The deflection image is valuable for this study because it simultaneously reveals large topographic features (the indent) and small features (cracks). Differential polishing of the alumina during preparation of the sample reveals some of the grain boundaries. When polished, some grains wear at a faster rate than others and this produces contrast at the grain boundaries. The cracks, highlighted by arrows, appear as sharp changes in contrast.

The geometric and mechanical characteristics of the coatings are listed in Table 3. The hardness and modulus data are consistent with values previously reported in the literature [40,41]. The calculated values of the fracture toughness are consistent with measurements of bulk materials, for which values vary between $2 \text{ GPa}\cdot\text{m}^{1/2}$ (for single crystals) to nearly $7 \text{ GPa}\cdot\text{m}^{1/2}$ (for some ceramic samples) [42,43]. Note that in each case, the harder coatings have shorter average crack lengths and this leads to higher calculated fracture toughnesses. In the present case, the measurements may be influenced by the thickness of the layers. For example, the modulus of the alumina layer is the smallest in coating 4, which is also the thinnest and may, therefore, be influenced the most by the underlying layers.

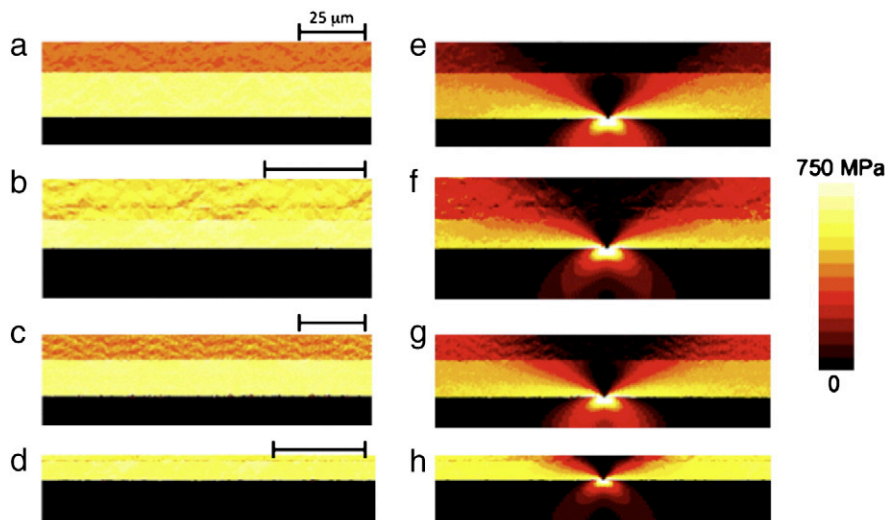


Fig. 4. The thermal stress distribution along the horizontal direction for the samples 1 through 4 without cracks (a–d) and the same samples with a crack (e–h). For each model, the scale bar on the left indicates a length of $25 \mu\text{m}$.

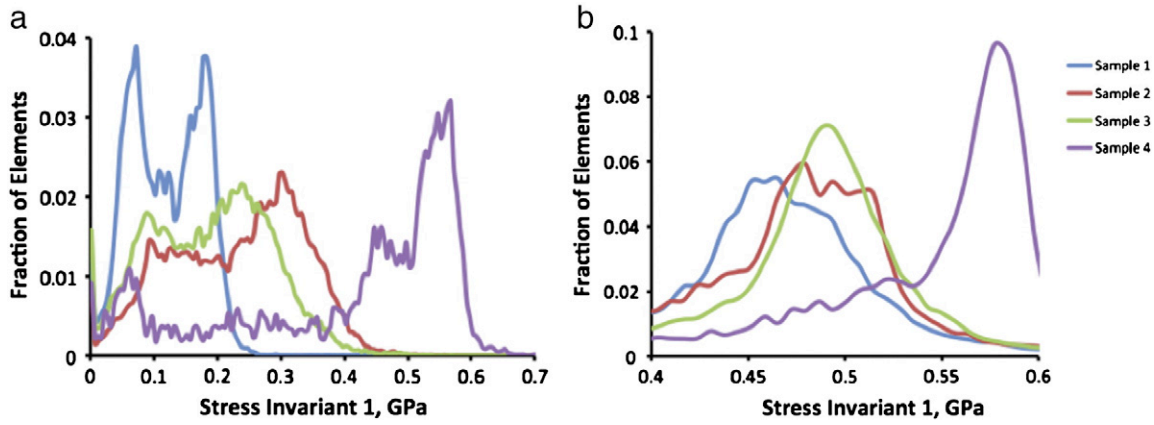


Fig. 5. Histogram of the values of the stress invariant 1 in (a) Al_2O_3 and (b) $\text{TiC}_x\text{N}_{1-x}$ (trace of the stress tensor) in each element for the four samples, based on the data in Fig. 4 (e–h). The legend in the right applies to both figures.

The distributions of stresses in the horizontal direction for each coating (with and without a channel crack) are shown in Fig. 4. In each case, there are abrupt changes in the stresses between the substrate (bottom), $\text{TiC}_x\text{N}_{1-x}$ (middle), and $\alpha\text{-Al}_2\text{O}_3$ (top) layers. In general, there is higher stress in the $\text{TiC}_x\text{N}_{1-x}$ layer than in the $\alpha\text{-Al}_2\text{O}_3$ layer. The data in Fig. 4 show that the stresses in the $\text{TiC}_x\text{N}_{1-x}$ layer are approximately 700 MPa while those in the alumina layers are 100 to 200 MPa lower. This is because the thermal expansion mismatch between the $\text{TiC}_x\text{N}_{1-x}$ layer and the substrate is larger than the mismatch between the $\alpha\text{-Al}_2\text{O}_3$ layer and the substrate. Both the microstructure of the sample and the cracks introduce heterogeneity in the distribution of stresses. The stresses in the parts of the coating closest to the crack are able to relax and the material furthest from the substrate can relax the most. Therefore, the overall stress relaxation is greater in the thicker coatings. However, there is an opposite effect on the substrate. Large tensile stresses are localized at the crack tip in the substrate and the thicker the film, the larger the extent of the stressed region.

To emphasize that there is a wide distribution of stresses and the distribution is not described by a simple functional form, histograms of the stresses in the $\alpha\text{-Al}_2\text{O}_3$ and $\text{TiC}_x\text{N}_{1-x}$ layers are shown in Fig. 5. The stresses in the alumina layer have multiple distinct maxima and the stresses in samples 2 and 3 are similar. Based on these data, it seems unlikely that it is possible to model the stress distributions in

different films by any simple functional form. Note that when Ma and Clarke [12] evaluated the residual stresses in polycrystalline alumina using piezospectroscopic methods, they found that for fine-grained alumina the average residual stresses from grain misorientations were about 100 MPa. This is comparable to stresses in the relaxed portions of the distribution (from material near the crack). The higher (unrelaxed) stresses in the coatings result from the strain imposed by the substrate.

The distribution of the elastic energy is shown in Fig. 6. The trends evident in these plots are similar to what is observed for the distribution of the stresses. Throughout most of the coating, the cracks reduce the amount of stored energy. However, in the region of the coating near the interface with the substrate, the elastic energy is actually larger than before the crack. So, in this localized region, the crack increases the stored elastic energy. Similar to the case of the stresses, the crack is more effective in reducing the average elastic energies in the thicker films. However, the high energy density region in the substrate and near the interface is larger in the thicker films.

A number of calculations were also carried out to examine how cracks interact as a function of crack spacing. Two models were considered, each consisting of a single $\text{TiC}_x\text{N}_{1-x}$ coating on a substrate with fixed width. The first coating was 4 μm thick and the second was 8 μm . In each model, cracks were situated so that there was a spacing of 10 μm , 30 μm , 50 μm , 70 μm , or 90 μm . The results

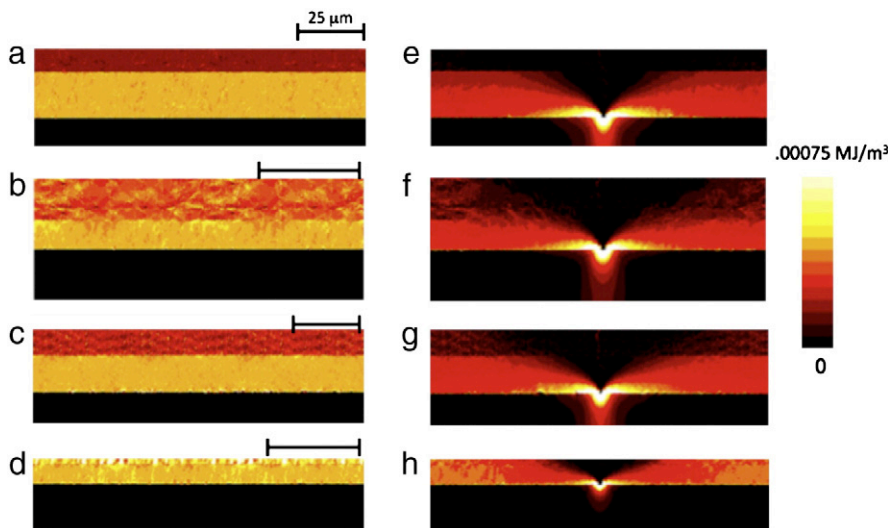


Fig. 6. The elastic energy distribution per element for samples 1 through 4 without cracks (a–d) and with a single crack in the center (e–h). All figures have the same scale.

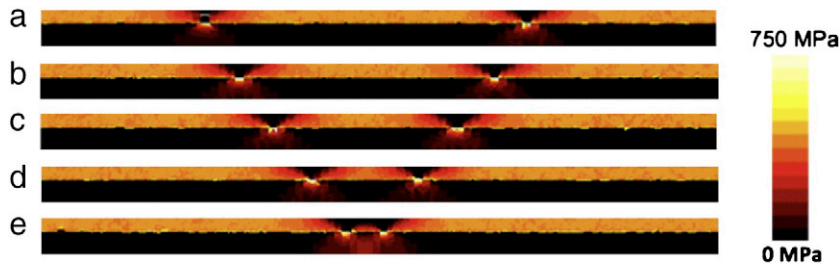


Fig. 7. Stress distribution as a function of crack spacing. Simulations are performed on 4 μm $\text{TiC}_x\text{N}_{1-x}$ coatings with crack spacing decreasing from 90 μm , 70 μm , 50 μm , 30 μm , to 10 μm shown in (a) to (e).

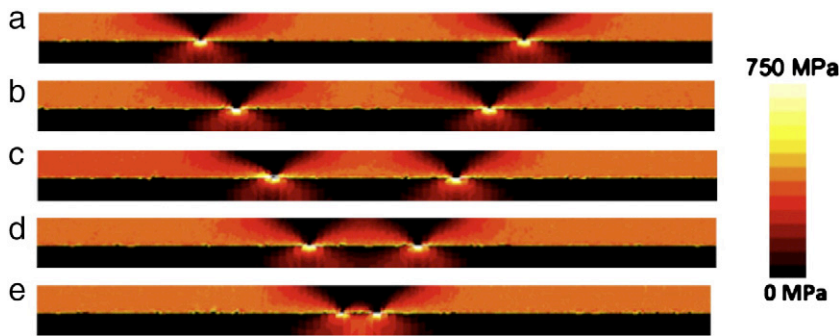


Fig. 8. Stress distribution as a function of crack spacing. Simulations are performed on 8 μm $\text{TiC}_x\text{N}_{1-x}$ coatings with crack spacing decreasing from 90 μm , 70 μm , 50 μm , 30 μm , to 10 μm shown in (a) to (e).

for the 4 μm thick coating are shown in Fig. 7 and the 8 μm thick coating are shown in Fig. 8. Note that, as pointed out above, the cracks relieve more stress in the thicker coating. Visually, the results suggest that each crack has a roughly fixed stress relieving capacity. However, when they are closer together, the overlap of stress relief zones reduces the total amount of stress relieved.

4. Discussion

One of the clearest results from the calculations is that the stress relaxation in coatings with cracks increases with the coating thickness. This is illustrated by Fig. 9, which plots the mean stress in each layer as a function of film thickness, for the cracked and uncracked coatings. The effect of thickness is more pronounced in the alumina layer than in the $\text{TiC}_x\text{N}_{1-x}$ layer. Note that for uncracked $\text{TiC}_x\text{N}_{1-x}$ layers, there is no change in stress with thickness. For the cracked layer, there is a modest decrease in stress as thickness increases. This is because the stress relief occurs near the walls of the crack and, for longer cracks in thicker layers, more stress is

relieved. A similar phenomenon occurs in the alumina layer, but is more dramatic; because the alumina layer is further from the constrained substrate/ $\text{TiC}_x\text{N}_{1-x}$ layer interface, it can relax more. Therefore, the decrease in stress with coating thickness is more dramatic for the cracked alumina coatings. There is also a decrease in stress with thickness for the uncracked alumina coatings and this is not necessarily expected. In this case, the lower stresses in samples 1 and 3 may be because these samples have the strongest texture [17]. The strength of texture in samples 1 and 3 (measured in multiples of a random distribution, MRD) are 8.8 and 6.8 MRD, respectively, while the strength of the texture in sample 2 and 4 is 4.2 and 5.2 multiples of random, respectively [17]. It has already been established that residual thermal stresses in alumina decrease with increasing texture [2,3].

It should be noted that there is actually a wide distribution of stresses, especially in the models with cracks. Here, we assume that the mean value is a representative quantity. This assumption is justified because past studies have shown that macroscopically measured properties are correlated to mean residual thermal stresses, which are

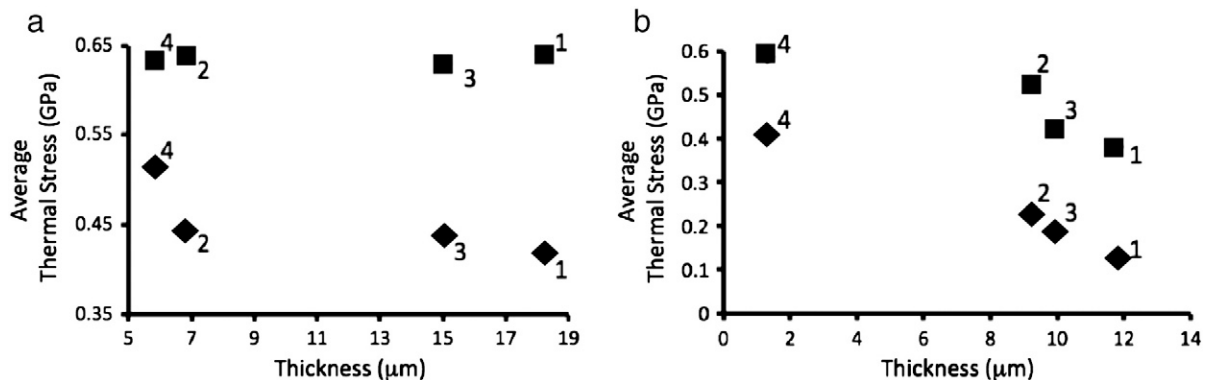


Fig. 9. Coating thickness versus residual thermal stress for (a) $\text{TiC}_x\text{N}_{1-x}$ and (b) $\alpha\text{-Al}_2\text{O}_3$. In each case, the numbers refer to the sample coating. These stresses were determined for the models in Fig. 4. The square symbols are for the coatings without cracks and the diamonds are for the coatings with cracks.

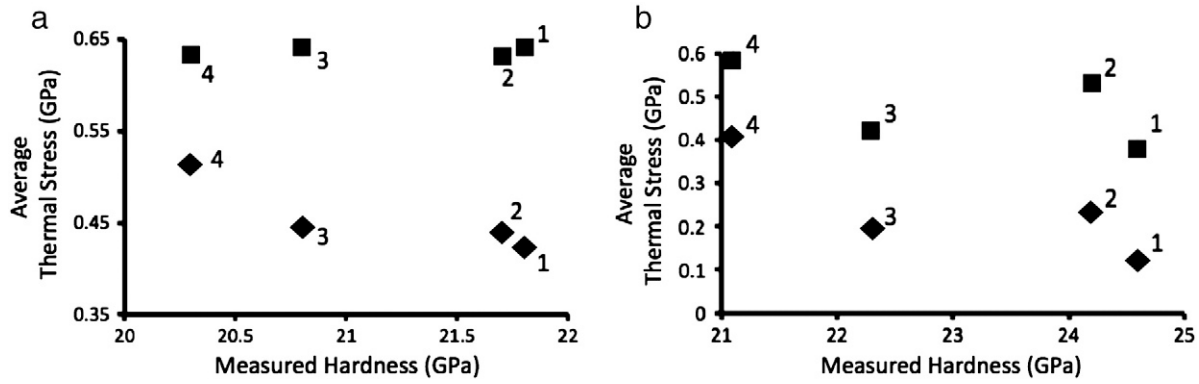


Fig. 10. Hardness versus mean residual thermal stress for (a) TiC_xN_{1-x} and (b) $\alpha-Al_2O_3$. In each case, the numbers refers to the sample coating. These stresses were determined for the models in Fig. 4. The square symbols are for the coatings without cracks and the diamonds are for the coatings with cracks.

usually the only quantitative metrics that are experimentally accessible [44].

The main hypothesis of this work was that the calculated thermal stresses could be correlated to measured coating properties, such as hardness. Again, we select the mean thermal stress as a metric and the relationship between the mean stress and the hardness of each layer is shown in Fig. 10. There are two important features of these results. The first is that for the simulations without cracks, the hardness of both coating layers is independent of thermal stress. For the TiC_xN_{1-x} layer without cracks, the thermal stress is almost the same for each layer. For the alumina layer, there are fluctuations, but no clear trend with hardness. The fluctuations in thermal stress in the alumina layer are likely related to differences in texture, as noted in the discussion of Fig. 9. The second feature is that for the simulations with cracks, there is a clear trend that increased hardness occurs in coatings that have lower calculated thermal stresses. The independence of the thermal stress and hardness in the crack-free coatings and the trend of increasing hardness with decreasing thermal stress in the cracked coatings suggest the importance of having some cracks to partially relieve stress and increase hardness. It is assumed that the inverse correlation between hardness and thermal stress persists within the range of geometric parameters (thickness and crack spacing) spanned by the four samples.

The simulations also explored the stress relieving capabilities of the cracks as a function of their separation. The mean stress in the coating as a function of separation is shown in Fig. 11. The average thermal stress in samples with a 10 μm crack spacing is the highest because of the overlap in the stress-relieving region. Because the regions overlap, the two cracks are relieving stresses in a smaller total area and this leads to higher average stresses. When the average crack separation reaches 50 μm , the thermal stress reaches the

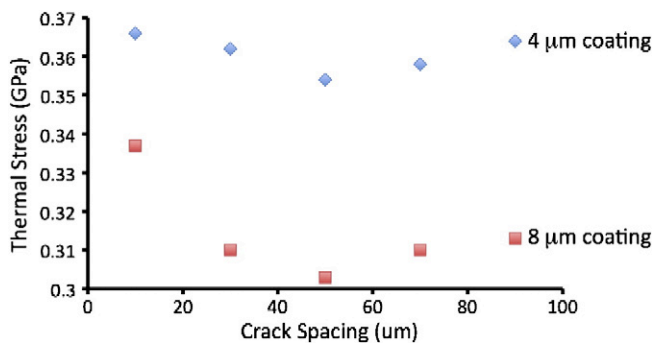


Fig. 11. Average thermal stress of TiC_xN_{1-x} coatings with different crack separations. Smaller crack separations result in higher thermal stresses. The lowest thermal stress occurs for the 50 μm crack separation.

smallest value, so cracks with this spacing relieve the most thermal stress. At larger separations, there is a small increase in stress. This is likely a result of the finite size of the simulation domain; as the cracks move closer to the fixed boundaries, they cannot relieve as much stress.

The results show that channel cracks in the coating relieve thermal stresses and this is correlated to improved hardness. While the idea that a coating with cracks is harder than one without is at first counter-intuitive, it must also be recognized that the coatings are under a tensile stress. Tensile stresses reduce a material's hardness [45] so anything that reduces the stress will mitigate its detrimental effects. The channel cracks reduce the tensile stress from the substrate and, therefore, lead to a relative increase in hardness. At some point, however, the cracks are also expected to have a negative impact on performance. If there are too many cracks, one would expect the coating to lack mechanical integrity. For example, if the regions of high elastic energy at the coating–substrate interface in Fig. 7 begin to overlap, the cohesion of the coating and the substrate would be affected. Second, it is clear that the cracks create tensile stresses in the substrate and this may promote cracking within the bulk of the tool bit insert. However, the extent of cracking in the present samples appears to still be in the region where it is beneficial, because the reduction of the thermal stresses by the cracks is correlated with increases in the hardness.

The thermo-elastic model employed here, which is formulated to be microstructurally accurate, allows residual thermal stresses to be calculated. These stresses are correlated to the observed hardness of the coating. This correlation makes it possible to seek improved materials by creating hypothetical microstructures and calculating the residual thermal stresses. Microstructures with lower stresses are expected to have higher hardness and would, therefore, be targets for synthesis. This procedure was already demonstrated for WC/Co composite structures [29,30]. While such investigations are beyond the scope of this study, the current work illustrates the relationship between mean residual thermal stresses and the hardness of the coating material.

5. Conclusions

Realistic, microstructure-based models of multilayer coatings on WC–Co substrates have been used to compute the thermal stress distribution. Channel cracks relieve stress in the coatings and this stress relief is more effective in thicker coatings. The residual thermal stresses are determined by the texture, thickness, and average crack spacing of the coating. The residual thermal stresses in the coating are inversely related to the hardness of the coating. This relationship provides guidance in the search for improved coatings.

Acknowledgment

This work was supported primarily by Kennametal Inc. and the Pennsylvania DCED. Partial support by the MRSEC program of the National Science Foundation under award number DMR-0520425 and the NSF REU program (DMR-0648976) is also acknowledged.

References

- [1] H.G. Prengel, W.R. Pfouts, A.T. Santhanam, *Surf. Coat. Technol.* 102 (1998) 183.
- [2] V.R. Vedula, S.J. Glass, D.M. Saylor, G.S. Rohrer, W.C. Carter, S.A. Langer, E.R. Fuller, *J. Am. Ceram. Soc.* 84 (2001) 2947.
- [3] H. Chien, Z. Ban, P. Prichard, Y. Liu, G. Rohrer, in: L.S. Sigl, P. Rodhammer, H. Wildner (Eds.), 17th Plansee Seminar, Plansee Group, Austria, 2009, p. 11.
- [4] H. Windischmann, *J. Vac. Sci. Technol. A* 9 (1991) 2431.
- [5] E. Chason, B.W. Sheldon, L.B. Freund, J.A. Floro, S.J. Hearne, *Phys. Rev. Lett.* 88 (2002) 156103.
- [6] Y.C. Tsui, T.W. Clyne, *Thin Solid Films* 306 (1997) 52.
- [7] J.G. Zhu, H.M. Xie, Z.X. Hu, P.W. Chen, Q.M. Zhang, *Surf. Coat. Technol.* 206 (2011) 1396.
- [8] P.A. Flinn, D.S. Gardner, W.D. Nix, *IEEE Trans. Electron Devices* 34 (1987) 689.
- [9] W.R. Lafontaine, C.A. Paszkiet, M.A. Korhonen, C.Y. Li, *J. Mater. Res.* 6 (1991) 2084.
- [10] J.W. Ager, M.D. Drory, *Phys. Rev. B* 48 (1993) 2601.
- [11] H. Windischmann, G.F. Epps, Y. Cong, R.W. Collins, *J. Appl. Phys.* 69 (1991) 2231.
- [12] Q. Ma, D.R. Clarke, *J. Am. Ceram. Soc.* 77 (1994) 298.
- [13] M. Levit, I. Grimberg, B.Z. Weiss, *Mater. Sci. Eng., A* 206 (1996) 30.
- [14] M. Toparli, O. Sayman, E. Celik, *Math. Comput. Appl.* 16 (2011) 125.
- [15] C.H. Hsueh, J.A. Haynes, M.J. Lance, P.F. Becher, M.K. Ferber, E.R. Fuller, S.A. Langer, W.C. Carter, W.R. Cannon, *J. Am. Ceram. Soc.* 82 (1999) 1073.
- [16] M. Lee, R.S. Gilmore, *J. Mater. Sci.* 17 (1982) 2657.
- [17] H. Chien, M.C. Gao, H.M. Miller, G.S. Rohrer, Z.G. Ban, P. Prichard, Y.X. Liu, *Int. J. Refract. Met. Hard Mater.* 27 (2009) 458.
- [18] T.W. Scharf, H. Deng, J.A. Barnard, *J. Vac. Sci. Technol. A* 15 (1997) 963.
- [19] E. Tam, P. Podsiadlo, E. Shevchenko, D.F. Ogletree, M.-P. Delplancke-Ogletree, P.D. Ashby, *Nano Lett.* 10 (2010) 2363.
- [20] M.T. Laugier, *J. Mater. Sci. Lett.* 4 (1985) 1539.
- [21] G.D. Quinn, R.C. Bradt, *J. Am. Ceram. Soc.* 90 (2007) 673.
- [22] S.A. Langer, E. Fuller, W.C. Carter, *Comput. Sci. Eng.* 3 (2001) 15.
- [23] S.A. Langer, A.C.E. Reid, S.I. Haan, R.E. Garcia, R.C. Lua, V.R. Coffman, OOF: Finite Element Analysis of Microstructures, National Institute of Standards and Technology (NIST), 2007. <http://www.ctcms.nist.gov/oof/>.
- [24] A.C.E. Reid, R.C. Lua, R.E. Garcia, V.R. Coffman, S.A. Langer, *Int. J. Mater. Prod. Technol.* 35 (2009) 361.
- [25] V. Cannillo, T. Manfredini, M. Montorsi, A.R. Boccaccini, *J. Non-Cryst. Solids* 344 (2004) 88.
- [26] R.E. Garcia, W.C. Carter, S.A. Langer, *J. Am. Ceram. Soc.* 88 (2005) 750.
- [27] R.E. Garcia, Y.M. Chiang, W.C. Carter, P. Limthongkul, C.M. Bishop, *J. Electrochem. Soc.* 152 (2005) A255.
- [28] A.D. Jadhav, N.P. Padture, E.H. Jordan, M. Gell, P. Miranzo, E.R. Fuller, *Acta Mater.* 54 (2006) 3343.
- [29] C.S. Kim, T.R. Massa, G.S. Rohrer, *Int. J. Refract. Met. Hard Mater.* 24 (2006) 89.
- [30] C.S. Kim, T.R. Massa, G.S. Rohrer, *J. Am. Ceram. Soc.* 90 (2007) 199.
- [31] R.O.E. Vijgen, J.H. Dautzenberg, *Thin Solid Films* 270 (1995) 264.
- [32] J.O. Kim, J.D. Achenbach, P.B. Mirkarimi, M. Shinn, S.A. Barnett, *J. Appl. Phys.* 72 (1992) 1805.
- [33] W.D. Kingery, *Introduction to Ceramics*, 2nd ed., John Wiley and Sons, New York, 1976.
- [34] D. Maouche, L. Louail, P. Ruterana, M. Maamache, *Comput. Mater. Sci.* 44 (2008) 347.
- [35] J.B. Wachtman, T.G. Scuderi, G.W. Cleek, *J. Am. Ceram. Soc.* 45 (1962) 319.
- [36] J.R. Gladden, J.H. So, J.D. Maynard, P.W. Saxe, Y. Le Page, *Appl. Phys. Lett.* 85 (2004) 392.
- [37] D.B. Hovis, A. Reddy, A.H. Heuer, *Appl. Phys. Lett.* 88 (2006) 1310.
- [38] A. Kelly, G.W. Groves, *Crystallography and Crystal Defects*, Longman, London, 1973.
- [39] W.M. Stoll, A.T. Santhanam, in: Kirk-Othmer Encyclopedia of Chemical Technology, John Wiley and Sons, 1992, p. 861.
- [40] D. Hochauer, C. Mitterer, M. Penoy, C. Michotte, H.P. Martinz, M. Kathrein, *Surf. Coat. Technol.* 203 (2008) 350.
- [41] E. Soderlund, I. Reineck, D.J. Rowcliffe, *J. Mater. Res.* 9 (1994) 1683.
- [42] B. Mussler, M.V. Swain, N. Claussen, *J. Am. Ceram. Soc.* 65 (1982) 566.
- [43] S.S. Smith, B.J. Pletka, in: *Indentation Fracture of Single Crystal and Polycrystalline Aluminum Oxide*, 1983, p. 189.
- [44] A. Zimmermann, E.R. Fuller, J. Rodel, *J. Am. Ceram. Soc.* 82 (1999) 3155.
- [45] Y.H. Lee, D. Kwon, *Scr. Mater.* 49 (2003) 459.